On the Strain Rate Sensitivity Measured by Nanoindentation at High Strain Rates

B.L. Hackett[1†], P. Sudharshan Phani[2], C.C. Walker[1], W.C. Oliver[3] and G.M. Pharr[1]

1. Texas A&M University, Department of Materials Science & Engineering, College Station, TX 77843, USA

2. International Advanced Research Centre for Powder Metallurgy & New Materials (ARCI), Balapur P.O., Hyderabad, Telangana, 500005, India

3. KLA Corporation, 105 Meco Ln, Oak Ridge, TN, 37830, USA

† Corresponding author: Benjamin L. Hackett
Email: bhackett@tamu.edu

Abstract

The flow stress of a material can be strongly dependent on the rate of applied strain. Measuring the strain rate sensitivity can reveal key insights into the mechanisms that drive plastic deformation. Indentation techniques have been developed to measure the strain rate sensitivity at quasistatic strain rates, but accessing higher strain rate regimes has been saddled with experimental and technical challenges. With state-of-the-art indentation instrumentation now capable of recording load and displacement at data acquisition rates in excess of 1.25 MHz, we report how strain rate sensitivity testing methodologies, especially those aimed for higher indentation strain rates, may be validated using the well-studied time-dependent deformation behavior of tungsten. The strain rate sensitivity for a (110) single crystal is shown to be consistent (m = 0.023 at 2 μm depth) across all tested strain rates and methods ranging from 10^{-2} - 10^{4} 1/s.

Keywords: nanoindentation; hardness; high strain rates; strain rate sensitivity; tungsten

1. Introduction

Strain rate sensitivity is a useful measure that can offer critical understanding of operative deformation mechanisms [1–3]. Many indentation-based techniques measuring the strain rate sensitivity and other time-dependent deformation properties of materials have been successfully developed and widely implemented [4]. However, such techniques have been experimentally limited to principally quasi-static strain rate regimes of less than 10^{-1} 1/s. As the interest in probing small-scale material deformation behavior at higher strain rates has increased, so has the requirement for improvements in instrumentation capable of accurately capturing the fast (sometimes < 200 μs) deformation processes [5–11]. It is not only technical improvements that have been necessary; serious attention to the applicability and validity of existing testing techniques in determining the properties of materials has also been desperately needed. Such new considerations must include the dynamic contribution of the instrument components required for the measurement of the displacement and the load on the sample. A detailed review of these factors is given by Phani *et al.* [12]. The limitations of standard methods used to determine even the most basic indentation properties must be re-examined for this new testing regime.

The most common techniques to determine the time-dependent deformation properties have been tests which carefully control the rates at which indentation deformation proceeds, ideally all while attempting to account for any potential underlying changes in a material's microstructure. A constant load and hold test (CLH) conveniently allows for the internal relaxation processes of the material to control the rate of continued deformation. The indentation strain rate for a CLH test is equivalent to the plastic creep rate. For indentation creep tests of this type, hold times are long so special care must be taken to account for thermal drift with modified methods, such as those that measure the contact stiffness through continuous stiffness measurement (CSM). Difficulty arises for CLH tests whereas the depth from creeping deformation during the hold increases, so does the contact area, thus leading to a decrease in contact pressure. This spoils the ability to directly compare the hardness as a function of strain rate under a steady state assumption.

A common testing procedure that attempts to fix the hardness and hence the underlying structural state involves loading at a constant indentation strain rate (CSR), achievable by proxy through either load-control constant loading rate to load ratio, $\dot{P}/P$ (CPP), or displacement-controlled instrumentation. The downside of such techniques is the need for multiple tests at varied strain rates to form the basis for probing time-dependent material properties. For a nonuniform or heterogeneous material, the intrinsic scatter from multiple tests can overwhelm the measurable effect. This can plague data where the sensitivity to changes in strain rate is low. To address issues of material heterogeneity and to increase testing throughput, multiple constant strain rates are used in making a single indent using abrupt changes between them. Strain rate jump tests (SRJ) have been used frequently, and not solely in indentation, to probe the time-dependent properties of materials. From a theoretical perspective, issues involving strain rate history effects, transients, and materials with a prominent depth component to hardness are still present with this technique.

All these methods suffer in a practical sense when the strain rate increases. The applied strain rate cannot be held constant in a load-controlled system with a defined control rate that has a comparable time scale to the actual test. It has been shown that such control loops begin to break down at ~ 100 1/s wherein the application of discrete force jumps begin to dominate the response and deviate from the ideally smooth and continuous force application [13]. For CLH tests, dynamic overloading prevents holding constant at the peak load. There are also numerous caveats involved with CSM that are amplified at higher rates of strain [14].

Nevertheless, it is not the aim of this work to necessarily address all of these outstanding issues that are present regardless of the strain rate regime tested, but rather, it is actually to use these existing methods as a basis to explore and validate new indentation instrumentation and techniques uniquely suited for measuring the strain rate sensitivity of materials at ranges well above 10^3 1/s. Specific treatment is given to two types of tests, impact and step load using a nanoindenter and piezoelectric load cell, each tailored specifically for high strain rate measurements. Combining techniques trusted in a quasistatic range grounded by physical contact area measurements of residual indents with tungsten, a BCC material whose time-dependent deformation properties at room temperature are considered to be an instantaneous function of strain rate [15], enables the validation of new methods. First, the testing methodology for strain rate sensitivity measurement is outlined with specific reference to adaptations for use at high strain rates. A baseline is set using CPP and CLH tests guided by a confirmation of the expected behavior of tungsten. The results of applying the new testing methodology at high indentation strain rates are discussed with reference to the baseline and critical method assumptions.

2. Materials and Experimental Methodology

2.1 Material Selection and Preparation

The material selected for this study is high purity 5N (110)-oriented single crystal tungsten (Surface preparation laboratory, Wormerveer, The Netherlands). The sample surface was prepared with standard grinding and polishing procedures (silicon carbide grinding pads with subsequent diamond slurry suspension polishing courses) with the final polishing step being a vibratory polish with 0.02 μm colloidal silica. Tungsten was selected as the material in this study because of its history-independent nature, which will be exploited for methodology validation. A single crystal specimen also eases interpretation of results by virtue of being more homogeneous and thus reducing test-to-test variation.

2.2 Instrumentation

All indentations were performed at 24 °C using a custom-built nanoindenter (KLA, Oak Ridge, TN) with a modified InForce 1000 actuator capable of recording fast contact deformation events with time of contact durations less than 200 μs. Displacement is acquired with laser interferometry simultaneously with a load signal output from a piezoelectric load cell (PCB Piezotronics, Inc., Depew, NY) at sample rates of 1.25 MHz. A schematic of the experimental setup is shown in Fig. 1. The load frame stiffness of the total system in series with the load cell is ~ 8 MN/m. The indentation testing was performed with a diamond Berkovich self-similar pyramidal indenter with four indents per test. Surface images of the residual indents were provided by a laser scanning confocal microscope (Keyence, Osaka, Japan). The precise area function of the tip was determined through standard calibration methods [16] on fused silica in a separate instrument (iMicro, KLA) afforded with continuous stiffness measurement.

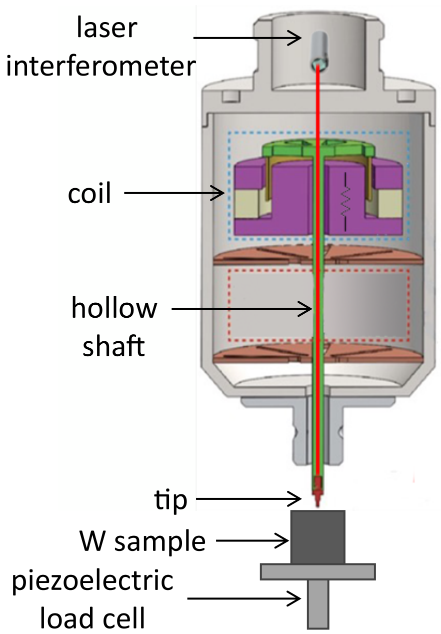

Fig. 1. Schematic of experimental setup with a purpose-built high strain rate capable actuator and piezoelectric load cell.

2.3 Testing Parameters and Theory

2.3.1 CPP and CLH tests

If hardness does not change substantially with depth, h, then the indentation strain rate for a self-similar pyramidal indenter may be defined as

$$\dot{\varepsilon}_i = \frac{\dot{h}}{h} \approx \frac{\dot{P}}{2P} \ . \tag{1}$$

CPP tests on single crystal tungsten were performed at equivalent $\dot{h}/h$ of 10^{-2}, 10^{-1}, 10^{0}, 10^{1}, and 10^{2} 1/s to a maximum target applied load of 1000 mN. To minimize thermal drift, the longest duration 10^{-2} and 10^{-1} 1/s tests were held on the surface adjacent to the test locations for an hour prior to the start of the tests. For the other tests, the measured drift rates < 1 nm/s were negligible in comparison to the time of contact of the tests. Sets of indentations loaded to a maximum static load of 1000 mN were made with CPP and CLH conditions. Once the maximum load was met for the CPP test, the load was unloaded in one second. For the CLH tests, the sample was first loaded at a $\dot{P}/P$ of 20 1/s; then, the load was held constant for 10 s at 500 mN before unloading completely in 1 s.

2.3.2 Impact and Step Load Tests

The impact test's full experimental and theoretical methodology is explained in detail in recent works by Hackett *et al.* [7] and Phani *et al.* [9]. The test begins by first finding the surface by an algorithm that begins by setting a stiffness threshold slightly above the stiffness of the column supporting springs. Once contact is made with the surface, the tip is withdrawn by a specific amount, set so that when a step force is subsequently applied to the electromagnetic coil, the time at which the velocity of the tip reaches a maximum coincides with contact with the surface. This condition of maximum velocity at the point of impact has been shown to be important for several reasons [9], but among the most practical is achieving the highest velocity, and hence maximizing the strain rates possible for a given initial coil force, F_0. The F_0 values for impacts used in this study and corresponding velocity upon surface contact are (20 mN, 8.83 mm/s) and (50 mN, 22.1 mm/s) respectively. The load on sample, P, may be determined with rearrangement of the following force balance equation,

$$m\ddot{h} + b\dot{h} + kh + P = F_0 \, , \tag{2}$$

where m, b, and k are the mass (9.72 g), damping coefficient ($0.135 \, \frac{\mathrm{N{\cdot}s}}{\mathrm{m}}$), and spring stiffness (478.5 $\frac{\mathrm{N}}{\mathrm{m}}$) respectively. A step load test proceeds in the same way as an impact test, just without pullback of the indenter. Once surface contact is established, the coil force is applied as a single step, and the following displacement and load signals are recorded. The F_0 values for step load tests are 200 and 500 mN.

2.3.3 Two Body Correction and Load Cell Calibration

All tests were performed in series with a piezoelectric load cell into which the sample was mounted. The piezoelectric load cell segment has a non-negligible effective mass, m_e, and independent motion that must be properly accounted for when analyzing the raw load signal. The effective mass was calculated by first isolating the stiffness of the load cell, $k_{\mathrm{LC}} = 11.2 \ \mathrm{MN/m}$, by finding the differential between the load frame stiffness with and without the load cell installed. Next, the dynamic resonant frequency, $f = 6900 \ \mathrm{Hz}$, of the second body, the load cell, was captured through FFT analysis. Then whereby

$$m_e = \frac{k_{\mathrm{LC}}}{(2\pi f)^2}, \tag{3}$$

the effective mass of the load cell was determined. The signal from the piezoelectric load cell, $P_{\text{raw-LC}}$, can then be reduced to its primitive component, an internal second body displacement, x_2, through

$$P_{\text{raw-LC}} = k_{\mathrm{LC}} \, x_2 \, . \tag{4}$$

From Eqns. 2-4, the true corrected load on sample is identified through the following relation that balances the acceleration, damping, and spring forces of the load cell:

$$P_{\text{2-Body}} = P_{\text{raw-LC}} - \left(-m_{\text{LC}} \frac{\ddot{P}_{\text{raw-LC}}}{k_{\text{LC}}} - b_{\text{LC}} \frac{\dot{P}_{\text{raw-LC}}}{k_{\text{LC}}}\right). \tag{5}$$

The damping coefficient, $b_{\text{LC}} = 40 \frac{\text{N·s}}{\text{m}}$, is manually fit to the logarithmic damping decrement. The two-body influence is magnified as the initial impact velocities increase with higher F_0. Without the two-body correction, there is a lag in the rise of the apparent load at the point of initial contact. Finally, the load cell is linearly calibrated to match the peak load from the displacement derivative method described in [7]. The advantage of using a calibrated and two-body-corrected piezoelectric load cell is that it largely sidesteps filtering artifacts that can plague the displacement derivative technique. The corrected load sourced from the load cell is the load displayed in all figures for the step and impact tests.

2.3.4 Indentation Measurements of Hardness, Strain Rate, and Strain Rate Sensitivity

The hardness is defined as

$$H = \frac{P}{A}, \tag{6}$$

where P is the load and A is the projected contact area supporting the load. In lieu of a way to assess the stiffness continuously throughout the test, a critical assumption of a constant ratio of the contact depth, h_c, to the total depth was made. Residual contact area measurements were made for all indents to join a true physical measurement of the deformed contact perimeter. Combined with the known area function of the tip, the value of h_c/h that solves the tip area function is

$$A = m_0 h_c^2 + m_1 h_c^1 + m_2 h_c^{\frac{1}{2}} + m_3 h_c^{\frac{1}{4}} + m_4 h_c^{\frac{1}{8}}. \tag{7}$$

Substituting in $\frac{h_c}{h}$ to Eqn. 7,

$$A = m_0 \left(h \frac{h_c}{h}\right)^2 + m_1 \left(h \frac{h_c}{h}\right)^1 + m_2 \left(h \frac{h_c}{h}\right)^{\frac{1}{2}} + m_3 \left(h \frac{h_c}{h}\right)^{\frac{1}{4}} + m_4 \left(h \frac{h_c}{h}\right)^{\frac{1}{8}} \tag{8}$$

with m_{0-4} as fit shape function coefficients for the geometry of the tip.

All indentation strain rates are expressed in an easily experimentally obtainable form, $\dot{\varepsilon}_i = \dot{h}/h$, suggested by Mayo and Nix [17]. Other definitions may be more suitable for comparison with conventional uniaxial compression creep testing [18–20]. Instantaneous strain rate values are computed from interpolation of the displacement-time derivative and displacement-time data at a particular depth for impact tests. A phenomenological constitutive expression relating stress, σ, and strain rate, $\dot{\varepsilon}$, that frequently describes the time-dependent behavior of many materials is a simple power law with m as the strain rate sensitivity and K a material constant is

$$\sigma = K\dot{\varepsilon}^{m}. \tag{9}$$

The strain rate sensitivity may be found from

$$\log\sigma = \log K + m\log\dot{\varepsilon} \tag{10a}$$

and

$$m = \frac{\partial\log\sigma}{\partial\log\dot{\varepsilon}}, \tag{10b}$$

the slope of a log-log plot of stress and strain rate. Translating stress into hardness can be easily accomplished with Tabor's empirical relation,

$$H = C\sigma_y\,, \tag{11}$$

which shows that hardness is simply linearly proportional to the flow stress via a constraint factor, C. For a fully plastic response, the constraint factor is ~ 2.8. Combining Eqn. 10a and 11 and substituting the indentation strain rate defined in Eqn. 1 for $\dot{\varepsilon}$, the indentation strain rate sensitivity is

$$m = \frac{\partial\log H}{\partial\log\dot{\varepsilon}_i}. \tag{12}$$

The conversion of Eqn. 9 into an indentation form involves the conversion of preexponential factors [20], but the power law exponent, m, is shared between both forms. However, it is important to acknowledge that for materials like polymers or glasses with a sizeable elastic component to the total deformation, the above analysis is not strictly applicable.

3. Results and Discussion

3.1 Constant Strain Rate Tests

The strain rate sensitivity is first established from CPP tests. The load-depth curves for the set of CPP tests are shown in Fig. 2a. The strong effect of strain rate hardening is readily apparent with the higher imposed indentation strain rates achieving higher loads compared across a common depth. In fact, a preliminary measure of strain rate sensitivity could be made by comparing the ratio of loads at a common depth since the load is proportional to the hardness.

$$m = \frac{\partial \log H}{\partial \log \dot{\varepsilon}_\iota} = \frac{\log(H_2/H_1)}{\log(\dot{\varepsilon}_2/\dot{\varepsilon}_1)} \approx \frac{\log(P_2/P_1)}{\log(\dot{\varepsilon}_2/\dot{\varepsilon}_1)} \tag{13}$$

An unusual cycling load-unload phenomenon materializes for the 10^2 1/s test. The cycle period corresponds to 1 ms, matching the control signal input rate of the instrument and confirming that as the source. The discrete results of the system attempting to maintain a constant $\dot{P}/P$ through exponentially increasing force steps form dynamic overloading events. The final and largest step eclipses the target load due to this overload. The dynamic load quickly relaxes to a quasistatic contact as the time derivatives of displacement trend toward zero. The remainder of the test resembles a constant hold and load test, which will be discussed in the following section. The load is only kept at the target load for a maximum of 6 ms, the time needed to send and receive the unloading signal and reduce the load on the sample. In that time, tungsten creeps forward even at the slightly reduced load. Second order polynomial equations were fit to the load-depth data of the tests for easy comparison and evaluation of the load at any given depth. The indentation strain rate of all these tests is plotted in Fig. 2b as a function of depth. Oscillations in the lower $\dot{P}/P$ tests come primarily from an interferometric displacement measurement error that amounts to a 3 nm peak amplitude sinusoidal oscillation with periodicity in displacement, not time, equivalent to a quarter of the laser wavelength (1550/4 ≈ 388 nm). This sinusoidal error when propagated to the derived quantity of indentation strain rate results in an absolute error amplitude that can be estimated by the product of the period of oscillation, the amplitude of the error in displacement, and the nominal strain rate. In terms of percent error, the amplitude of the humps is 4.8% of the nominal strain rate. Notwithstanding the humps induced by the controller and cyclical laser interferometry error, the strain rates during the loading segments match the nominal rates.

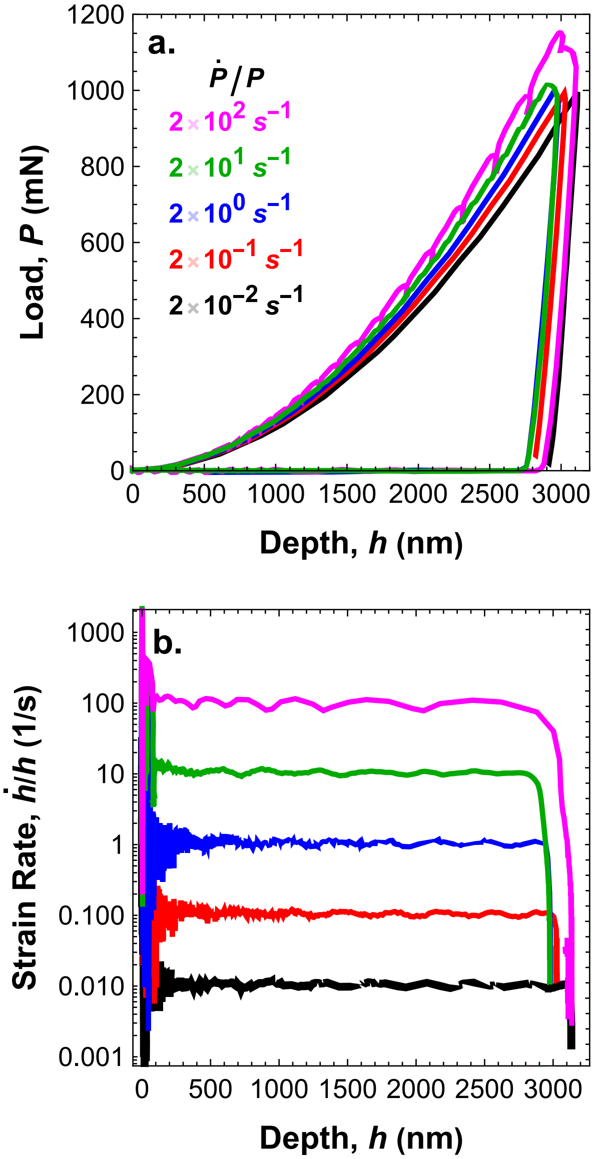

Fig. 2a. (110) tungsten load and depth curves for all CPP tests 2b. Indentation strain rate for all CPP tests as a function of depth demonstrating the steadiness of $\dot{h}/h$.

Arriving at a physically meaningful and grounded hardness for these CPP tests is important for validation, so each indent's physical contact area was determined. A representative 2×10^{-2} 1/s $\dot{P}/P$ indent is shown in Fig. 3 with the contact periphery used to calculate the area outlined.

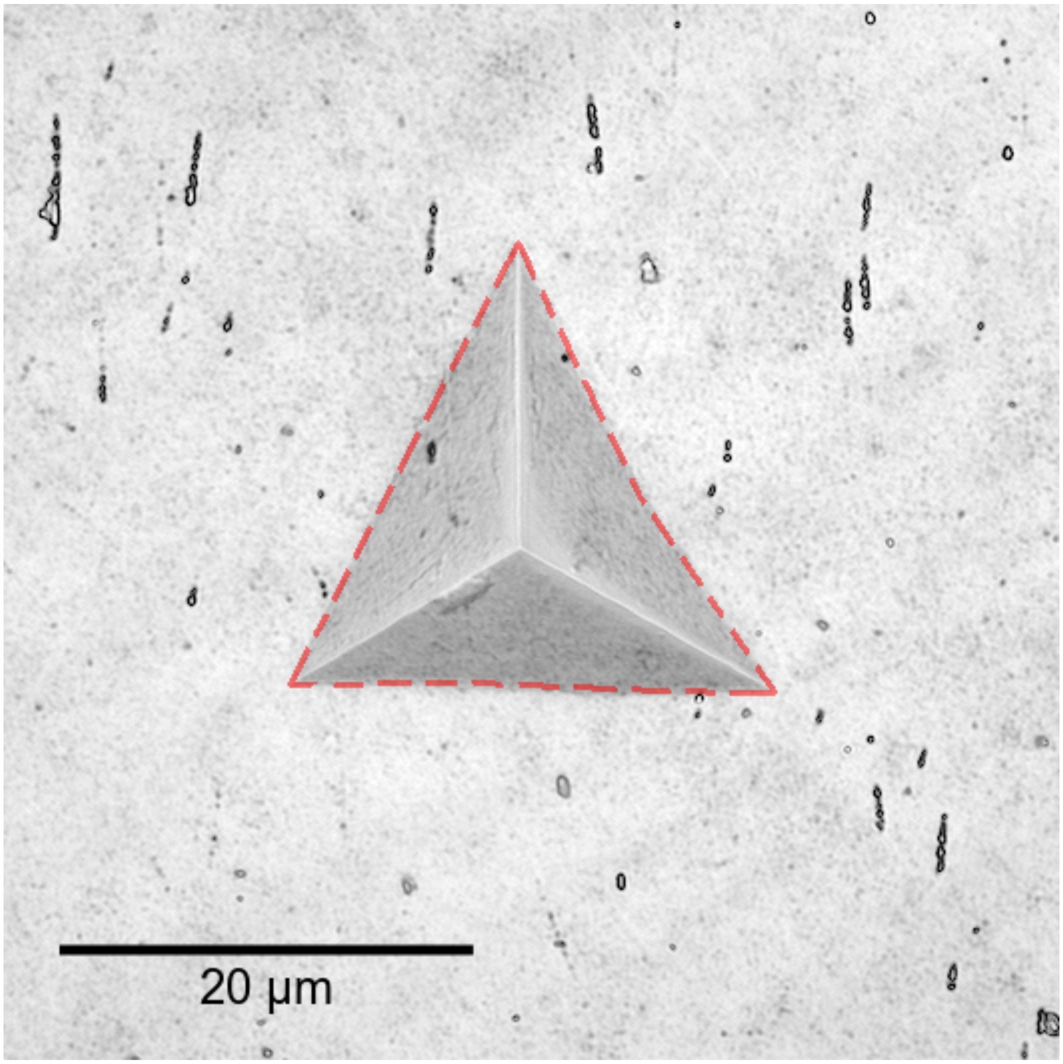

Fig. 3. Laser confocal image of the 2×10^{-2} 1/s $\dot{P}/P$ test with outlined contact perimeter.

The corresponding strain rates for these tests must take into consideration the slowdown in velocity, and hence a decrease in strain rate, as the maximum load is met. The departure from the nominal strain rate at the end of loading complicates analysis of the size of the residual indents. The effect is magnified when there is a greater difference between the nominal strain rate and the relaxation rate and time. Essentially, the strain rate may fall off so quickly that a steady equilibrium state is not achieved. Hardness derived from physical measurement of residual contact areas is provided in Fig. 4. There is a minimal relaxed depth and size difference of the lowest strain rate CPP test, so this test was used for subsequent analysis. The effective contact depth to total depth ratio was found to equal 1. This value is used for all tests to calculate the contact area and hardness according to Eqn. 6 and Eqn. 8 as a function depth. A non-linearity that correlates with the increasing amount of relaxation as the strain rate increases can be readily observed when a comparison is made to unrelaxed data. Unrelaxed hardness measurements were taken at a depth of 2 µm during loading, and a model fitted to these measurements is represented by the dashed line in Fig. 4.

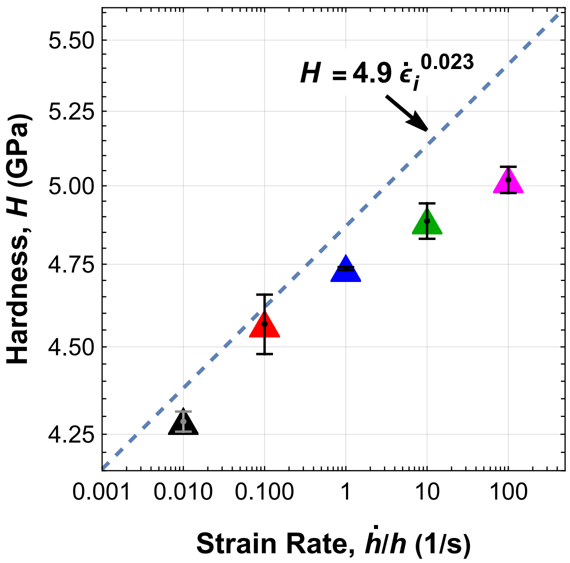

Fig. 4. Hardness derived from physically measured residual contact areas and the maximum achieved load for CPP tests. The dashed line represents a model fit to hardness at a depth of 2 μm and uninfluenced by relaxation.

3.2 Constant Load and Hold Tests

The load and strain rate as a function of depth of CLH tests are shown in Fig. 5a and 5b. A similar story of relaxation creep is observed during the hold, except in this case, the strain rate sensitivity may be directly obtained from this hold and underscores the direct relation between the hardness and current strain rate of tungsten. Hardness as a function of instantaneous strain rate is included in Fig. 6. The slope derived from the holding period on the log-log plot is m and is 0.023. The influence of any size effect is expected to be small, in part because of the limited displacement (about 200 nm) during the hold and the fact that the size effect is greatly diminished at 2 μm.

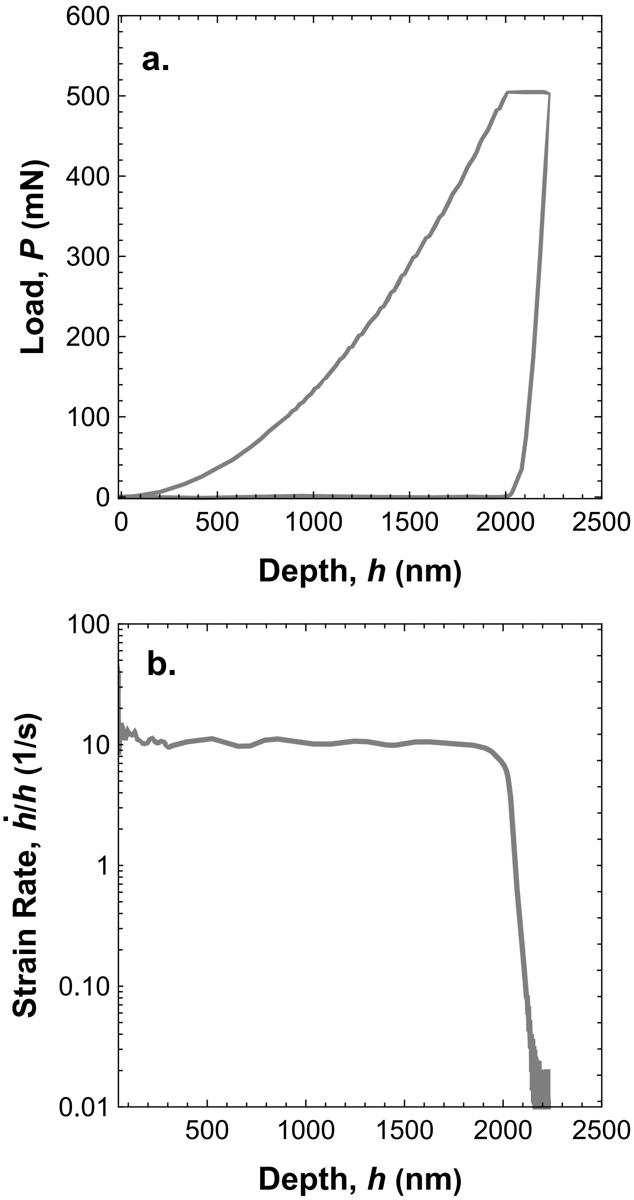

Fig. 5a. (110) tungsten load and depth curves for a CLH test 5b. Indentation strain rate for a CLH test as a function of depth during the hold.

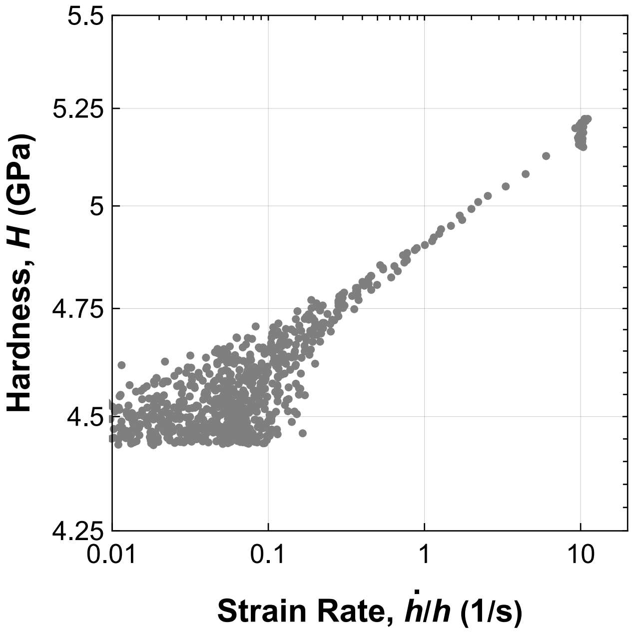

Fig. 6. Hardness versus strain rate during the holding portion of a CLH test that starts with loading at a strain rate of 10 1/s.

3.3 High Strain Rate Impact Tests and Step Load Tests

The resulting load and depth of the impact and step load tests of the tungsten sample are found in Fig. 7a for various F_0. Slight nosing of the load depth curves near the maximum load reflects the abrupt decrease in strain rate at the end of loading. The imposed strain rate as a function of depth is shown in Fig. 7b with the dynamic nature of the impact and step load tests observed in the variation of strain rate during a test.

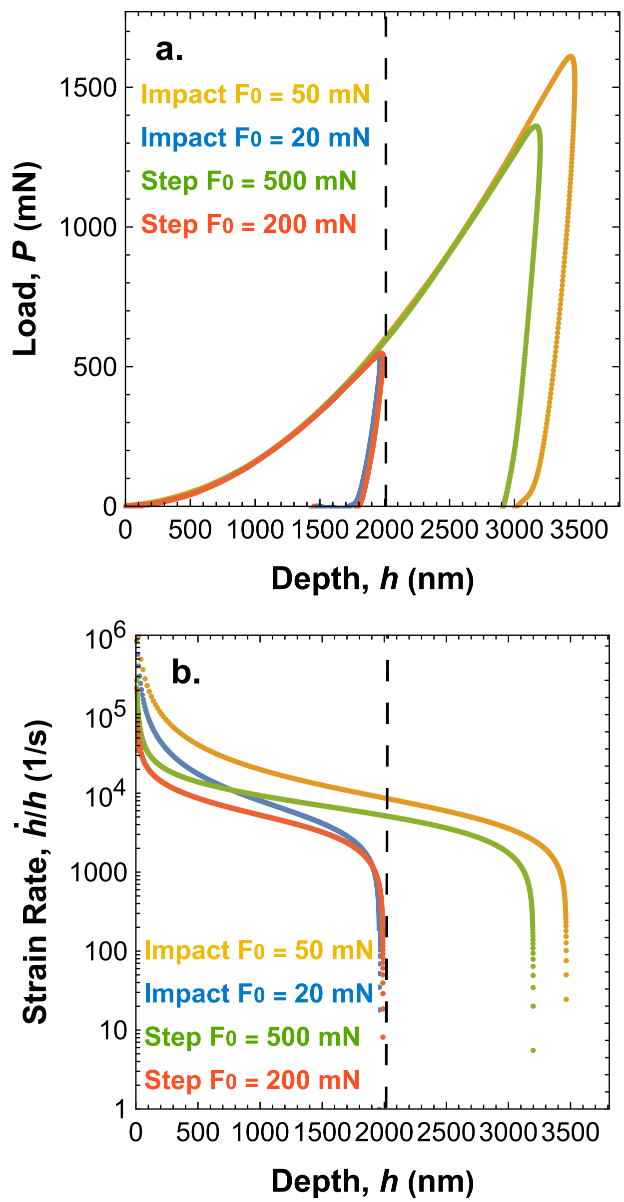

Fig. 7a. Load and depth curves from the high indentation strain rate impacts and step load tests. 7b. The course of dynamically changing strain rates applied to the sample as a function of depth for impact and step load tests. The intersecting vertical dashed line indicates the 2 μm comparison depth.

Hardness is evaluated at the same depth to properly compare all the test methods and exclude contributions to changes in hardness from depth dependencies. Since the strain rate changes continuously as a function of depth for impact and step load tests, the instantaneous value at a depth of 2 μm during loading is represented in the values given in Fig. 8.

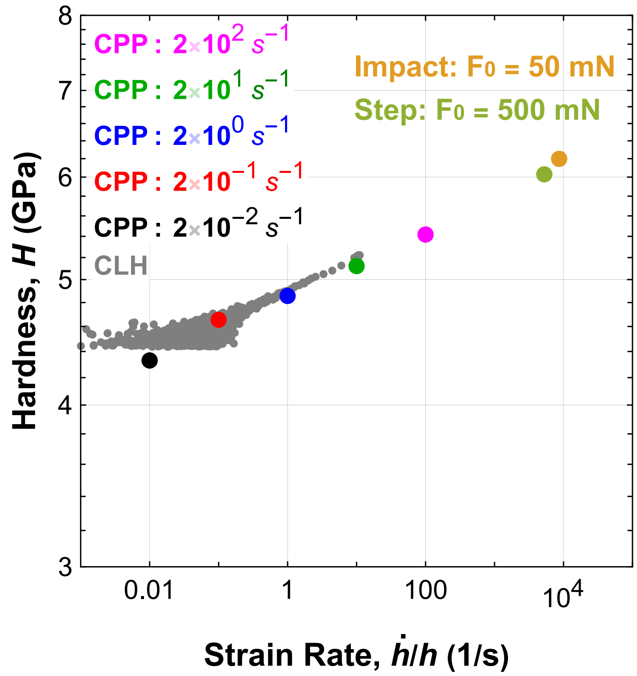

Fig. 8. Hardness and instantaneous strain rate at 2 μm for all test types (CPP, CLH, impact, and step load).

The most important takeaway from Fig. 8 is that the trend of hardness and strain rate established by the CPP tests on tungsten extends to both impact and step load tests at much higher strain rates, and thus it provides additional confidence that the specific testing methodology employed here is a satisfactory one for m determination at strain rates greater than 10^3 1/s. The strain rate sensitivity from indentation found here ($m = 0.023$) agrees very well with the range of values in literature 0.02-0.03 [21,22].

3.4 Critical analysis of testing assumptions

3.4.1 Hardness and contact depth without CSM

Indentation hardness is typically defined as the ratio of the peak load applied and the contact area under that load. While the peak applied load is easily known with high precision, even in the case of an impact, measuring the true contact area under load, especially a dynamic one, is less straightforward. CSM is now a common technique that can be used to estimate the contact area, an improvement over the traditional Oliver-Pharr method, which is principally limited to cases where the contact surface pile-up is negligible [16,23]. As the rate of loading increases, instrument and theoretical limits are met and do not allow CSM to function correctly as it is normally implemented with a lock-in amplifier. The working oscillation amplitude and frequency are outside a detectable range. Without the ability to use CSM to estimate the contact area, a solution is offered that combines physical measurements of the indents, a well-calibrated tip area function, and an assumption of a constant ratio of the contact depth to the total depth of penetration. The last factor must be scrutinized in cases where a blunt tip encounters a material with low E/H. In this case, at low depths where the blunting is most severe, the character of the indentation becomes more elastic, and thus h_c/h can approach the elastic limit, $2/\pi$. For most metals loaded past an initial pop-in that signals the start of plastic processes, this is not an issue. If the strain hardening rate is a strong function of strain rate, then h_c/h could change based on the effect strain hardening has on pile-up [24].

It is critical for the measurement of hardness to only consider the projected contact area that supports load. Since pile-up occurs when displaced material plastically flows up to the unconfined surface surrounding the indent, the contact area may include regions along its periphery that are piled-up, yet still support load from the indenter. In single crystal specimens, pile-up hillocks may extend outward to areas that do not support load. The boundary of deformed load-bearing material which conformed to the shape of the tip while in contact outlines the apparent contact area used to determine h_c/h. 'Apparent' in this context refers to the contact area as determined from an image of a residual indent. The actual h_c/h is dependent on the true area of the contact at full load, though the difference between it and the apparent contact area is simply a multiplicative factor. The difference has no bearing on measuring strain rate sensitivity, but it will impact the conversion of the preexponential term in Eqn. 9. The main consideration is only that there is a specific h_c/h, which ties a physical area to the measured depth, so the contact depth and associated tip area can be ascertained from the total depth alone. Hardness determined in this way is unrestricted by any loading rate limits and, therefore, can be used to provide an indentation hardness value continuously at every recorded datum for any loading schedule, whether that be constant strain rate, constant load and hold, impact, or a step load. This technique is valid regardless of the amount of pile-up or sink-in because contact areas are directly measured. It is true that simply observing the end result of an indentation after unloading cannot provide direct insight into the exact contact area under load due to the sometimes unintuitive motion of surface points, which muddles the picture upon unloading, especially for materials with large amounts of elastic recovery. Finite element studies may offer additional value here. Nevertheless, physical measurements of residual indent areas shown in Fig. 4 provide a consistent basis from which to ground hardness values. With a way to determine hardness using a constant ratio of h_c/h being established, there still may remain concerns that the rate of strain is not constant.

3.4.2 Instantaneous Strain Rate for Impact and Step Load Tests

This section discusses the appropriate strain rate for impact and step load testing and the implications of the measured hardness values. For an impact test, the advance of the penetrating tip is naturally resisted and halted by the material itself. This dictates that the strain rate decreases as a function of time and depth of penetration. This process becomes even more complicated by the coupling of the instrument system which serves to drive the tip into the specimen. Because of this decrease, the changing strain rate must be accounted for in some way. Certain averaging schemes have been developed which take the strain rate at the midpoint or consider the average velocity [6,25]. Other strategies have involved discrete integration of the strain rate curves as a function of either time or depth. It is disconcerting that these methods do not yield a unifying factor. This may indicate that the very idea of an average or effective indentation strain rate might be untenable, especially when considering the consistent trend in strain rate sensitivity shown in Fig. 8 using instead the concept of the instantaneous strain rate at a common depth. It should be noted that the successful application of the instantaneous strain rate definition in this study may be due to the lack of history dependence.

3.4.3 Strain Rate History Independent Deformation Properties of Tungsten

The strain rate sensitivity of BCC metals has generally been found to be closely related to the process of kink pair production and propagation against the background of a highly energetic landscape of potential energy [26,27], i.e., Peierls potential. Overcoming the short-range scope of this barrier is a thermally activated process which may be phenomenologically described by Eqn. 9, a power law equation with constant value of strain rate sensitivity across many decades of strain rates. It is a phenomenon that reflects material behavior linked to the frequency at which those processes can occur. This near instantaneous movement of dislocations in response to an applied stress is related to the strain rate through Orowan equation, $\dot{\varepsilon} = \rho b \bar{v}$,which contains the key idea that a density of mobile dislocations, ρ , moving within a material with Burgers vector, b, accommodates the strain rate by collectively moving at an effective velocity, $\bar{v}$. It should be no surprise that this resistance to deformation, which may be associated with the measurement of hardness, would likewise be related to the instantaneous strain rate in a test. Changes in longer range in athermal contributors to the total hardness, i.e. structural sensitivity to strain rate, such as what has been observed in FCC metals [28,29], are reflected by changes in m as a function of $\dot{\varepsilon}$. Combining the known nature of BCC metals at low strain rates, e.g., the nature of the thermal activation to overcome the Peierls stress and the comparatively insignificant contribution of substructural development via direct dislocation interaction and production-annihilation processes, single crystal tungsten acts as an ideal model material to assess strain rate sensitivity techniques. It also guides what strain rates ought to apply for impact and step load tests and what the hardness represents for a constant structure assumption. Given that all test values using the techniques outlined in this study converge to the same power law exponent, $m = 0.023$, it strongly suggests that the well-documented behavior of BCC tungsten [30] is reproduced, even at indentation strain rates greater than 10^3 1/s.

3.4.4 Effect of the indentation size effect on SRS measurements

As seen in Fig. 9, a major factor that can affect comparisons of hardness at different strain rates is the indentation size effect.

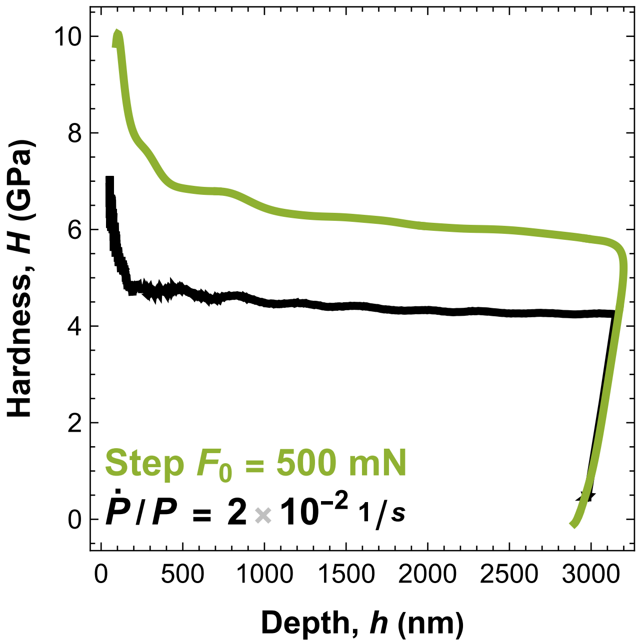

Fig. 9. A comparison of the indentation size effect between a step load and a CPP test.

A common depth of 2 μm was used to compare all the tests at the various strain rates. This was done to neutralize the indentation size effect. Previous studies have indicated that in BCC metals, the size effect appears to be purely an additive quantity and separate from the relationship between strain rate and the hardness [31,32]. The reason for this simple additive property leads to the postulated reasons for the indentation size effect itself. The effect is now beginning to be understood as having multiple components which themselves operate at different length scales [33–35]. Starting with a damage free surface, the resistance to initial deformation may be predicated on the availability of dislocation sources and the ease at which new dislocations can be multiplied from them to accommodate the imposed strain from the indenter. Geometrically necessary dislocation density trends lower at greater depths, and the interplay of the development of the plastic zone with associated dislocation substructures and the self-similarity of the indent geometry inevitably gives rise to the observed decrease in hardness as indent depth increases [36].

In this study, the long-range dislocation mechanisms in tungsten inducing the indentation size effect shown in Fig. 9 appear to occur regardless of the strain rate those present dislocations must satisfy, agreeing with prior experimental work [26,32,37,38]. Thus, there is a clear separation between the indentation size effect and the thermally activated process that mediates plastic flow rates for BCC metals. In the first, the strength increase is sourced from higher dislocation density, and in the second, the increase in strength is from thermal limitations on the velocity of dislocations. This understanding coupled with the observation of a constant strain rate sensitivity value across all tested strain rates implies that there is no additional storage of dislocation line length or an upset in the balance between the generation and annihilation of dislocations. For this to be the case, the Peierls stress must be large, as in BCC metals like tungsten [39].

4. Conclusions

The measurement of strain rate sensitivity at strain rates exceeding 10^3 1/s is laden with many experimental and theoretical challenges. In this work, some of these issues were systematically addressed by exploiting well-established time-dependent deformation properties of BCC single crystal tungsten. Conventional CPP and CLH tests in concert with physical measurement of residual indent contact areas at a quasistatic indentation strain rate provided a common trusted baseline from which to validate key components of higher strain rate testing methodology applied to impact and step load tests with a purpose-built high strain rate nanoindenter. The critical aspects of the method included:

1. Using the instantaneous value of the indentation strain rate
2. Linking the hardness to an assumed constant h_c/h found by a directly measured final contact area and known tip area function
3. Comparing indentation strain rate and hardness at a common depth

A constant power law strain rate relationship, independent from the indentation size effect, was shown to exist for single crystal tungsten at low strain rates and extending to all tested strain rates with $m = 0.023$ after applying the above assumptions, positively supporting the validity of their usage. Wider applicability of these principles to probe other materials, such as those with strain rate history dependent behavior is an appealing potential avenue for future study.

Acknowledgements

This work was supported by the Department of Energy, National Nuclear Security Administration under Award no. DE-NA0003857.

Conflict of Interest

On behalf of all authors, the corresponding author states that there is no conflict of interest.

References

1. V. Maier-Kiener and K. Durst, JOM **69**, 2246 (2017).
2. A. A. Elmustafa, S. Kose, and D. S. Stone, J. Mater. Res. **22**, 926 (2007).
3. K. Durst and V. Maier, Curr. Opin. Solid State Mater. Sci. **19**, 340 (2015).
4. P. Sudharshan Phani, W. C. Oliver, and G. M. Pharr, JOM **69**, (2017).
5. G. Guillonneau, M. Mieszala, J. Wehrs, J. Schwiedrzik, S. Grop, D. Frey, L. Philippe, J. M. Breguet, J. Michler, and J. M. Wheeler, Mater. Des. **148**, 39 (2018).
6. C. Zehnder, J. N. Peltzer, J. S. K. L. Gibson, and S. Korte-Kerzel, Mater. Des. **151**, 17 (2018).
7. B. L. Hackett, P. Sudharshan Phani, C. C. Walker, W. C. Oliver, and G. M. Pharr, J. Mater. Res. **170**, 105105 (2023).
8. P. Sudharshan Phani and W. Oliver, Materials (Basel). **10**, 663 (2017).
9. P. S. Phani, B. L. Hackett, C. C. Walker, W. C. Oliver, and G. M. Pharr, J. Mech. Phys. Solids **170**, 105105 (2023).
10. D. T. Casem, J. J. Pittari, and J. J. Swab, Conf. Proc. Soc. Exp. Mech. Ser. **1**, 63 (2022).

11. M. Hassani, D. Veysset, K. A. Nelson, and C. A. Schuh, Scr. Mater. **177**, 198 (2020).
12. P. Sudharshan Phani, B. L. Hackett, C. C. Walker, W. C. Oliver, and G. M. Pharr, Curr. Opin. Solid State Mater. Sci. **27**, 101054 (2023).
13. B. Merle, W. H. Higgins, and G. M. Pharr, J. Mater. Res. (2019).
14. G. M. Pharr, J. H. Strader, and W. C. Oliver, J. Mater. Res. **24**, 653 (2009).
15. G. Taylor, Prog. Mater. Sci. **36**, 29 (1992).
16. W. C. Oliver and G. M. Pharr, J. Mater. Res. **19**, 3 (2004).
17. M. J. Mayo and W. D. Nix, Acta Metall. **36**, 2183 (1988).
18. A. F. Bower, F. N.A., N. A., and O. N., Proc. R. Soc. London. Ser. A Math. Phys. Sci. **441**, 97 (1993).
19. G. Kermouche, J. L. Loubet, and J. M. Bergheau, Mech. Mater. **40**, 271 (2008).
20. C. Su, E. G. Herbert, S. Sohn, J. A. LaManna, W. C. Oliver, and G. M. Pharr, J. Mech. Phys. Solids **61**, 517 (2013).
21. A. K. Zurek and G. T. Gray, Le J. Phys. IV **01**, C3 (1991).
22. H. W. Schadler, Acta Metall. **12**, 861 (1964).
23. W. C. Oliver and G. M. Pharr, J. Mater. Res. **7**, 1564 (1992).
24. B. Taljat and G. M. Pharr, Int. J. Solids Struct. **41**, 3891 (2004).
25. H. Somekawa and C. A. Schuh, J. Mater. Res. **27**, 1295 (2012).
26. D. Brunner, Mater. Trans. **41**, 152 (2000).
27. H. Conrad, JOM **16**, 582 (1964).
28. P. S. Follansbee and U. F. Kocks, Acta Metall. **36**, 81 (1988).
29. P. S. Follansbee and G. T. Gray, Mater. Sci. Eng. A **138**, 23 (1991).
30. T. Dümmer, J. C. Lasalvia, G. Ravichandran, and M. A. Meyers, Acta Mater. **46**, 6267 (1998).
31. X. Qiu, Y. Huang, W. D. Nix, K. C. Hwang, and H. Gao, Acta Mater. **49**, 3949 (2001).
32. Z. Y. Liang and G. M. Pharr, J. Mech. Phys. Solids **165**, 104935 (2022).
33. X. Ma, W. Higgins, Z. Liang, D. Zhao, G. M. Pharr, and K. Y. Xie, Proc. Natl. Acad. Sci. U. S. A. **118**, 1 (2021).
34. G. M. Pharr, E. G. Herbert, and Y. Gao, Annu. Rev. Mater. Res. **40**, 271 (2010).
35. T. A. Parthasarathy, S. I. Rao, D. M. Dimiduk, M. D. Uchic, and D. R. Trinkle, Scr. Mater. **56**, 313 (2007).
36. W. D. Nix and H. Gao, J. Mech. Phys. Solids **46**, 411 (1998).
37. V. Maier, C. Schunk, M. Göken, and K. Durst, Philos. Mag. **95**, (2015).
38. J. Wang, T. Volz, S. M. Weygand, and R. Schwaiger, J. Mater. Res. **36**, 2166 (2021).
39. B. G. Butler, J. D. Paramore, J. P. Ligda, C. Ren, Z. Z. Fang, S. C. Middlemas, and K. J. Hemker, Int. J. Refract. Met. Hard Mater. **75**, 248 (2018).